A Full-Range ZVS Comprehensive Control Strategy for Dual-Port LLLC Induction Heating System

Qixiang Yang, Fujun Ma, *Senior Member, IEEE*, Zhengxiao Zhang, Junpan Wang, Gelin Huang, Rui Fan, Quanjie Li, and Zhiheng Tong

***Abstract*—The full-range zero voltage switching (ZVS) comprehensive control strategy is proposed for a high-power dual-port *LLLC* induction heating system which allows the system to operate efficiently across the entire power range. Under heavy load, a novel dual-phase-shift (DPS) control strategy is proposed in this article. Using time-domain analysis, the minimum circulating current curve and the ZVS range under DPS conditions are derived. The optimal phase-shift angle relationship is determined by combining the minimum circulating current and the full-range ZVS region. However, under DPS control, the minimum output power is one-quarter of its full load capacity due to the lack of internal phase-shift in inverter II. To overcome this limitation, a frequency-doubling pulse frequency modulation (FD-PFM) control strategy is proposed under light load. Frequency-doubling control is implemented through time-division multiplexing between the two inverters, which enables the resonance circuit frequency to be doubled without altering the switching frequency of each inverter. The FD-PFM approach facilitates a faster response to power variation with frequency, enabling the system to adjust power in a narrower frequency range. This enables smooth, wide-range power adjustment across the entire system and ensures ZVS operation across the full power range. A 14 kW prototype was developed, and the experimental results align closely with the theoretical analysis.**

***Index Terms*—Dual-phase-shift (DPS), frequency-doubling pulse frequency modulation (FD-PFM), full-range zero voltage switching (ZVS), induction heating (IH).**

I. INTRODUCTION

INDUCTION heating (IH) systems are widely used in both household and industrial heat treatment applications, owing to their numerous advantages, including high efficiency, environmental friendliness, flexible control, and rapid heating rates [1]. In industrial applications, the power required by IH power supplies is typically large. Moreover, the output power of the heating system must be adjustable within a specific range to ensure effective control of the workpiece heating temperature [2], [3].

Methods for increasing the capacity of IH power supplies currently include the parallel connection of multiple power switches and inverter parallel configurations with high-frequency transformers on the load side [4]. To enhance the output capacity of high-frequency power modules, the parallel connection of multiple power switches is a commonly adopted approach [5]. However, prolonged parallel operation of multiple power switches may result in issues such as device drive desynchronization, uneven current distribution, and potential device failures [6], [7]. In addition to increasing power through the parallel connection of multiple switches, large power output can also be achieved by paralleling multiple modules and loads [8]. A topology for a multi-phase IH system is proposed in [9], in which multiple current-type resonant inverters utilize a phase-shift angle coordination control method to enable multicoil power supply and large power output. In [10], a system involving multiple voltage-source half-bridge inverters connected in parallel is proposed. However, the use of a half-bridge configuration and an *LC* resonant circuit limits the system's ability to output high power. A phase-angle control method in a zone control induction heating (ZCIH) system is introduced in [11], the system consists of separate working coils and multiple inverters. The ZCIH system controls the current amplitude of each coil to ensure uniform temperature distribution across the workpiece, however, the coupling between the load coils complicates independent power control for each inverter. In [12], a multiphase resonant inverter system that incorporates multiple coupled coils for IH applications was proposed. The system employs a phase-shift control strategy for power regulation. However, the use of half-bridge inverters limits the system's capacity to deliver high power, and mutual interference between the coils complicates its performance.

In high-frequency, high-power resonant systems, reducing switching losses and minimizing low electromagnetic interference noise can significantly enhance system efficiency. Therefore, achieving zero voltage switching (ZVS) for the power switches is particularly crucial [13]. However, the ZVS operation range of system is narrow during power control, especially in systems with multiple inverters operating in parallel. Therefore, achieving ZVS during parallel power control of multiple inverters remains a critical area of research [14]. Mainstream control strategies for IH systems include phase-shift modulation (PSM) [15], pulse-frequency modulation (PFM) [16], and pulse-density modulation [17]. PFM control is associated with an inherent technical issue: the limitation of switching frequency at medium to low output power levels [18], which restricts the ability to achieve a wide range of power regulation for

---

Received 6 February 2025; revised 23 April 2025; accepted 7 June 2025. Date of publication 11 June 2025; date of current version 5 August 2025. This work was supported by Delta Power Electronics Science and Education Development Program Fund under Grant DREK2024004. Recommended for publication by Associate Editor O. Lucia. *(Corresponding author: Fujun Ma.)*

The authors are with the College of Electrical and Information Engineering, Hunan University, Changsha 410082, China (e-mail: mafujun2013@hnu.edu.cn).

Color versions of one or more figures in this article are available at https://doi.org/10.1109/TPEL.2025.3578628.

Digital Object Identifier 10.1109/TPEL.2025.3578628

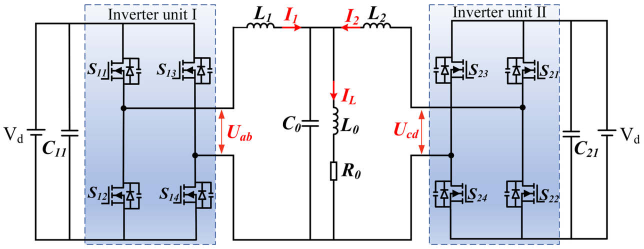

Fig. 1. Circuit diagram of the dual-port *LLLC* Topology.

the IH load. In contrast, PSM control is characterized by a narrow soft-switching range during power adjustment [19]. An asymmetrical voltage-cancellation control control method, proposed in [20], resolves the issue of the narrow soft-switching range during the phase-shift process, however, it results in a higher turn-OFF current, thereby increasing overall power losses. In [8], an IH power supply system composed of multiple inverters connected in parallel was proposed. The system employs an adjust pulse density modulation (APDM) control strategy for power regulation, enabling full-range ZVS operation, however, under light load conditions, the APDM control strategy may cause intermittent current. In [21], a system employing two half-bridge resonant inverters in parallel is introduced to enhance output power, the power regulation of the system is achieved through a dual-pulse modulation strategy. However, at lower power levels, circulating currents gradually increase, leading to a reduction in system efficiency.

To achieve both high-power output and full-range ZVS operation with high efficiency, a comprehensive full-range ZVS control strategy for high-power *LLLC* IH system is proposed in this article. Under heavy load conditions, a novel dual-phase-shift (DPS) control strategy is employed, frequency-doubling pulse frequency modulation (FD-PFM) control strategy is applied for light load conditions. The DPS strategy involves phase-shifting between the two inverters as well as between the diagonal power switches of inverter I. The proposed comprehensive control strategy ensures full-range ZVS operation across the entire power range, thereby optimizing system efficiency. The rest of this article is organized as follows. Section II introduces the topology resonant circuit parameters, and operating modes of the dual-port *LLLC* IH systems. Section III describes the implementation of a novel DPS strategy and the achievement of full-range ZVS. Section IV describes the principle of FD-PFM strategy. Section V validates the proposed control strategy through experimental results. Finally, Section VI concludes this article

II. DPS DUAL-PORT *LLLC* TOPOLOGY AND PRINCIPLE

A. *Dual- Port* LLLC *Topology*

Fig. 1 illustrates the topology of the dual-port *LLLC* IH system. The dual-port *LLLC* resonant circuit is composed of two identical matching inductors L_1 and L_2 , a load coil L_0, and a matching capacitor C_0. R_0 representing the equivalent resistance of the load coil.

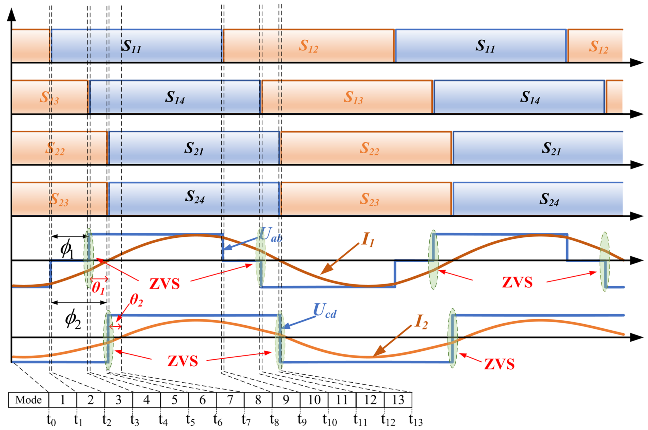

Fig. 2. Waveform of the output voltage and current of the two inverters.

The equivalent impedance expression of the dual-port *LLLC* resonant circuit is given by

$$Z = \frac{1}{j\omega C_0 + 1/(j\omega L_0 + R_0)} + \frac{1}{1/j\omega L_1 + 1/j\omega L_2} \tag{1}$$

where $L_1 = L_2$

$$\omega_o = \sqrt{\frac{2L_0 + L_1}{C_0 L_0 L_1}}. \tag{2}$$

The quality factor Q of a resonant circuit is defined as

$$Q = \frac{\omega_o L_0}{R_0} = \frac{1}{R_0} \times \sqrt{\frac{(2L_0 + L_1){L_0}^2}{C_0 L_0 L_1}}. \tag{3}$$

The inductance matching coefficient β of an *LLLC* resonant circuit is defined as

$$\beta = L_1/L_0. \tag{4}$$

In the case of no phase-shift, the initial phase angle difference θ between the output voltage and current of a dual resonant inverter is given by

$$\theta = \arctan\left(\frac{2+\beta}{2Q}\right). \tag{5}$$

B. *Analysis of Operating Modes*

The operating waveforms of the DPS *LLLC* IH system are presented in Fig. 2. In this figure, θ_1 denotes the phase angle between the output voltage and current of inverter I, θ_2 represents the phase angle between the output voltage and current of inverter II, ϕ_1 refers to the internal phase shift angle of inverter I, and ϕ_2 indicates the phase shift angle between inverter I and inverter II. The output power regulation is achieved by adjusting the phase shift angles ϕ_1 andϕ_2.

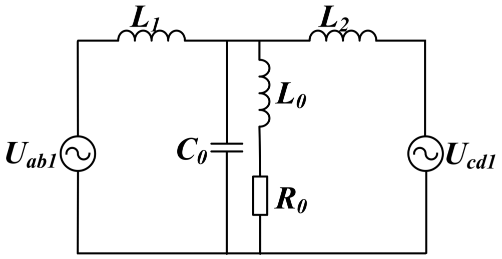

Fig. 3. Frequency domain equivalent circuit based on fundamental frequency AC voltage source.

III. IMPLEMENTATION OF DPS CONTROL STRATEGY AND FULL RANGE ZVS

A. *Voltage-Current Frequency Domain Analysis of DPS Control*

Ignoring the dead-time and edge resonance interval, the fundamental components of the output voltages U_{ab} and U_{cd} of inverters I and II in Fig. 1 can be expressed using a Fourier series as follows:

$$\begin{cases} U_{ab1} = \frac{4V_d}{\pi}\cos(\frac{\phi_1}{2})\sin\left(\omega(t - t_{\phi_1/2})\right) \\ U_{cd1} = \frac{4V_d}{\pi}\sin\left(\omega(t - t_{\phi 2})\right) \end{cases} \tag{6}$$

where $\omega = 2\pi f_s$ and f_s represents the switching frequency

$$\begin{cases} \dot{U}_{ab1} = V\cos(\frac{\phi_1}{2})e^{-j\frac{\phi_1}{2}} \\ \dot{U}_{cd1} = Ve^{-j\phi_2} \end{cases} \tag{7}$$

$$V = 2\sqrt{2}V_d/\pi. \tag{8}$$

Fig. 3 shows the equivalent circuit in the frequency domain for the fundamental component. and represent the fundamental components of the square wave voltage (complex vectors), respectively.

By applying the superposition principle to the equivalent circuit in Fig. 3, the current phasors I_1 and I_2 of the two resonant circuits can be expressed as follows (9) shown at the bottom of this page.

As shown above, the current magnitude and phase, and thereby the power, can be adjusted by changing the dual phase-shift.

Fig. 4 shows the equivalent circuit of the system derived by Thevenin's theorem, where the system's equivalent ac voltage phasor U_0 can be defined as follows:

$$U_0 = \left(V\cos\left(\frac{\phi_1}{2}\right)e^{-j\frac{\phi_1}{2}} + Ve^{-j\phi_2}\right)/2. \tag{10}$$

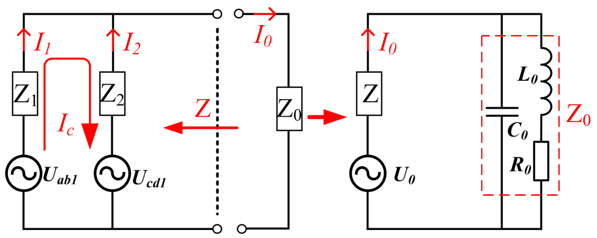

Fig. 4. Equivalent circuit diagram.

The equivalent impedance Z is given by

$$Z = j\omega L/2 \tag{11}$$

where$L = L_1 = L_2$.

The inductive heating load current I_0 can be obtained from Fig. 4

$$\dot{I}_0 = \dot{I}_1 + \dot{I}_2 = \frac{\dot{U}_0}{\dot{Z} + \dot{Z}_0} \tag{12}$$

$$\begin{cases} \dot{I}_0 = \frac{V(2Q - j(2+\beta))\left(\cos(\phi_2) + \cos(\frac{\phi_1}{2})[\cos(\frac{\phi_1}{2}) - \sin(\frac{\phi_1}{2})] - \sin(\phi_2)\right)}{QR_0\beta^2} \\ L_0 = \frac{QR_0}{\omega}; L_1 = L_2 = \frac{QR_0\beta}{\omega}; C_0 = \frac{2+\beta}{QR_0\beta\omega}. \end{cases} \tag{13}$$

The output voltage of the inverter bridge is denoted as U_0, while the voltage across the load resonant capacitor is U_c. The voltage gain of the *LLC* resonant load is given by, (14) show at the bottom of the next page

When $\omega = \omega_0$, $H_u(\omega_0)$ is

$$H_u(\omega_0) = -(2 + 2jQ)/\beta. \tag{15}$$

When$\omega = \omega_0$, the phase angle of the voltage gain is

$$\varphi_u = \arctan\left(\frac{-2Q/\beta}{2/\beta}\right) \approx -\frac{\pi}{2}. \tag{16}$$

From (16), it can be observed that the resonant capacitor voltage U_c always lags behind the inverter output voltage U_0 in phase. At $\omega = \omega_0$, the phase difference φ_u is approximately $-90°$. Moreover, the phase difference φ_u exhibits a monotonic changing near ω_0. Therefore, during phase-locked loop(PLL) control, φ_u should be chosen as the control variable.

At the resonant frequency, the capacitive voltage U_c and equivalent supply voltage U_0 of the system maintain a constant 90° phase difference. However, U_0 cannot be directly utilized for PLL, the capacitive voltage U_c and the voltage U_{cd} of inverter II are employed for PLL implementation. As shown

$$\begin{cases} I_1 = \frac{V(-j\cos(\phi_1) + \sin(\phi_1))(A\cos(\frac{\phi_1}{2})^2 + B\cos(\phi_2) + C\cos\left[\frac{\phi_1}{2}\right]\sin\left[\frac{\phi_1}{2}\right] + D\sin(\phi_2)}{\omega(jL_1R_0 + jL_2R_0 - 2\omega L_0L_1 - \omega L_1L_2 - j\omega^2C_0L_1L_2R_0 + \omega^3C_0L_0L_1L_2)} \\ I_2 = \frac{V(\cos(\phi_2) + j\sin(\phi_2))(Ecos(\frac{\phi_1}{2})^2 + F\cos(\phi_2) + G\cos\left[\frac{\phi_1}{2}\right]\sin\left[\frac{\phi_1}{2}\right] + H\sin(\phi_2)}{\omega(jL_1R_0 + jL_2R_0 - 2\omega L_0L_1 - \omega L_1L_2 - j\omega^2C_0L_1L_2R_0 + \omega^3C_0L_0L_1L_2)} \\ A = jR_0 - \omega L_0 - \omega L_2 - j\omega^2C_0L_2R_0 + \omega^3C_0L_0L_2; B = -jR_0 + \omega L_0; \\ C = R_0 + j\omega L_0 + j\omega L_2 - \omega^2C_0L_2R_0 - j\omega^3C_0L_0L_2; D = -R - j\omega L_0 \\ E = -R_0 - j\omega L_0; F = R_0 + j\omega L_0 + j\omega L_1 - \omega^2C_0L_1R_0 - j\omega^3C_0L_0L_1; \\ G = jR_0 - \omega L_0; H = -jR_0 + \omega L_0 + \omega L_1 + j\omega^2C_0L_1R_0 - \omega^3C_0L_0L_1; \end{cases} . \tag{9}$$

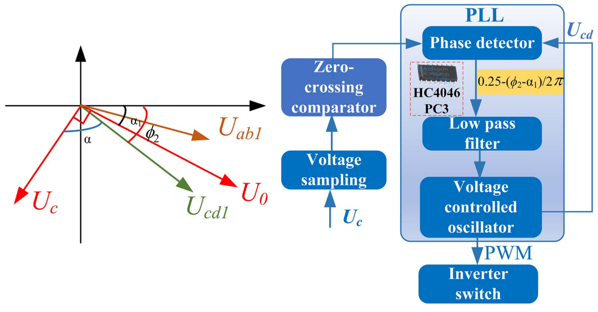

(a) (b)

Fig. 5. PLL schematic diagram. (a) Voltage vector diagram. (b) Composition of PLL.

in Fig. 5(a), U_{ab1} represents the fundamental output voltage vector of inverter I, while U_{cd1} corresponds to the fundamental output voltage vector of inverter II. Since inverter II operates without internal phase shifting, U_{cd1} consequently remains in phase with U_{cd}. The phase angle between U_c and U_{cd} is given by $90° - (\phi_2 - \alpha_1)$. The PLL synchronization requires

$$\alpha = 90 - (\phi_2 - \alpha_1). \tag{17}$$

In this formula, α_1 represents the angle of the IH system's equivalent voltage U_0, and α is the angle between the capacitor voltage U_c and the output voltage U_{cd} of inverter II. Therefore, maintaining the relationship in (17) during the phase shift process serves as the phase-locking condition.

Fig. 5(b) presents the block diagram of the PLL, which comprises a phase detector (PD), a low-pass filter, and a voltage-controlled oscillator [22]. The inputs to the PD are the capacitor voltage U_c and the output voltage U_{cd} of inverter II.

B. Calculation of the Circulating Current

The circulating current I_c can be expressed as shown in the equivalent circuit in Fig. 4

$$I_c = \frac{\dot{U}_{ab1} - \dot{U}_{cd1}}{2\,\dot{Z}_L} = \dot{I}_1 - \dot{I}_2 \tag{18}$$

where $\dot{Z}_L = \dot{Z}_1 = \dot{Z}_2$, the value of the circulating current can be calculated as follows:

$$\begin{aligned}|I_c| = {}& -\frac{V^2}{2{R_0}^2 Q^2 \beta^4}(G + H\cos\phi_1 + I\cos(\phi_1 - 2\phi_2)\\
&+ J\cos(\phi_1 - \phi_2) + K\cos[2(\phi_1 - \phi_2)]\\
&+ L\cos(2\phi_1 - \phi_2) + M\cos(\phi_2) + NQ\beta)^{\frac{1}{2}}\\
G = {}& -4 - 4Q^2 - 2\beta - \beta^2\\
H = {}& 2\beta + \beta^2; I = 2+2Q^2; J = 2+2Q^2+2\beta; K = 2+2Q^2\\
L = {}& 1 + Q^2 + \beta; M = 3-3Q^2-3\beta; N = -2\sin(\phi_1-\phi_2)\\
&+ \sin(2\phi_1 - \phi_2) - \sin(\phi_2)\end{aligned} \tag{19}$$

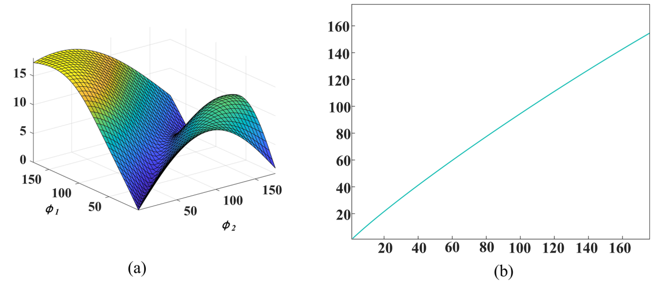

(a) (b)

Fig. 6. Variation of circulation with phase shift angle. (a) Relationship between circulating current and dual-phase-shift. (b) Optimal circulating current curve.

where (19) defines the value of the circulating current I_c. When $Q = 15$ and $\beta = 10$, the circulating current varies with the phase shift angle, as shown in Fig. 6(a).

Fig. 6 illustrates the variation of circulating current magnitude with phase shift angles ϕ_1 and ϕ_2. As seen in Fig. 6(a), the circulating current reaches a minimum when the phase-shift angles satisfy a specific relationship. The projection of this minimum circulating current curve onto the plane of the two phase-shift angles is shown in Fig. 6(b), with the corresponding curve relationship described by

$$\phi_1 = 0.8857\phi_2. \tag{20}$$

When the two phase-shift angles satisfy the relationship described by (20), the circulating current of the entire system operates at its minimum state.

C. Calculation of Power

Based on (9), show at the bottom of this page, the output powers P_1 and P_2 of inverters I and II are given by the following formulas:

$$\begin{cases} P_1 = \dfrac{V^2\cos(\frac{\phi_1}{2})\left(Q\cos(\frac{\phi_1}{2}) + Q\cos\left(\frac{1}{2}(\phi_1 - 2\phi_2)\right) + \sin\left(\frac{1}{2}(\phi_1 - 2\phi_2)\right)\right)}{QR_0\beta^2} \\ P_2 = \dfrac{V^2(2Q + Q\cos(\phi_1 - \phi_2) + Q\cos(\phi_2) - \sin(\phi_1 - \phi_2) + \sin(\phi_2))}{2QR_0\beta^2} \end{cases} \tag{21}$$

$$\begin{aligned}P_0 &= P_1 + P_2; P_{\max} = 2V^2/R\beta^2; P_{\min}\\ &= V^2/2R\beta^2 = 0.25P_{\max}.\end{aligned} \tag{22}$$

Here, P_1 represents the output power of inverter I, P_2 represents the output power of inverter II, P_0 is the total output power of the system, $P_{\max}$ is the maximum output power, and $P_{\min}$ is the minimum output power after the completion of the DPS.

Fig. 7 shows the power diagram of the system. According to (21) and the figure, P_1 decreases as the dual phase-shift angle increases, eventually reaching zero. Similarly, P_2 also decreases

---

$$H_u = \frac{U_c}{U_0} = \left(\frac{2L_2\left(R_0 + j\omega L_0\right)}{\left(-L_2\left(R_0 + j\omega L_0\right) + L_2R_0\left(-1 + \omega^2 C_0 L_2\right) + j\omega L_1\left(-L_2 + L_0\left(-1 + \omega^2 C_0 L_2\right)\right)\right)}\right). \tag{14}$$

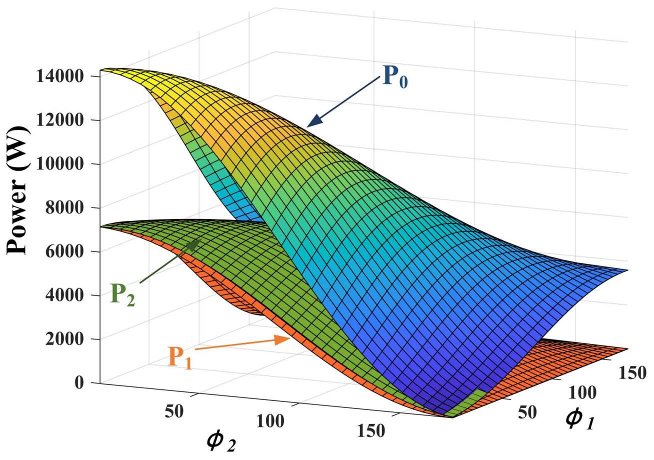

Fig. 7. Relationship between output power and phase shift angle.

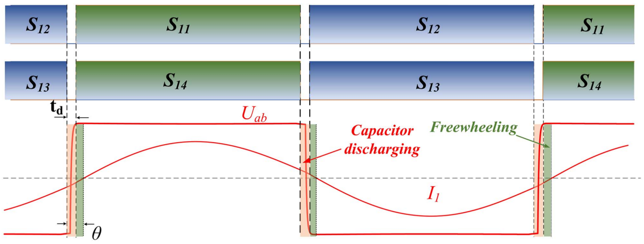

Fig. 8. Waveforms of the inverter in the switching process.

continuously with an increase in the dual phase-shift angle. However, since inverter II does not have an internal phase-shift angle, the system power, as described by (22), ultimately decreases to $0.25P_{\max}$ after the completion of the dual phase-shift. In summary, the system's output power decreases as the dual phase-shift angle increases.

D. Realization of Full-Range ZVS

In the control of a dual-port full-bridge inverter, using either internal phase-shift within the inverter or inter-phase shifting between the two inverters results in a narrow ZVS operating range. This leads to hard switching of the power devices, causing significant switching losses. The optimal DPS control strategy is introduced in this section.

To achieve ZVS operation, the IH system must be operated in an inductive state. When the snubber circuit and dead-time are negligible, the critical condition for achieving ZVS operation when the phase angle θ between the voltage and current is equal to 0°. However, power transistors have intrinsic output capacitancesand besides, lossless snubber circuits are commonly used to reduce voltage spikes during the switching of power transistors [23]. In this design, a 150 pF snubber capacitor is connected in parallel with each SiC MOSFET.

As shown in Fig. 8, during the dead time t_d , the capacitor C_s must be fully discharged to achieve ZVS operation. Therefore, there exists a minimum dead time denoted as $T_{\min}$. The angle corresponding to the minimum dead time $T_{\min}$ is defined as $\theta_{\min}$, and $T_{\min}$ [24] can be obtained from

$$T_{\min} = \frac{\theta_{\min}}{\omega_0} = \frac{1}{\omega_0}\cos^{-1}\left(1 - \frac{2\omega_0 C_s V_d}{I_m}\right) \tag{23}$$

where ω_0 is the resonant frequency, V_d is the input voltage of the inverter, C_s is the snubber circuits capacitor, and I_m is the magnitude of the inverter output current.

ZVS is achieved by first conducting the antiparallel diode before turning ON the switch, thereby ensuring that the drain-source voltage is clamped to zero. To ensure ZVS operation for the switch, it is necessary to ensure that the current continues to flow through the antiparallel diode when the switch is turned ON. As shown in Fig. 2, the following conditions must be satisfied to achieve ZVS

$$I_{1(t_3)} < I_{\beta\min}; I_{1(t_{10})} > I_{\beta\min}; I_{2(t_5)} < I_{\beta\min}; I_{2(t_{12})} > I_{\beta\min} \tag{24}$$

where $I_{\beta\min}$ is the minimum current required to realize the ZVS operation.

Because of symmetry, analysis of the negative half-cycle is unnecessary. During the phase-shifting process, ZVS can be achieved if the output voltage and current of each inverter remain in an inductive state, where the current consistently lags behind the square wave of the output voltage. In (25), θ_1 and θ_2 denote the phase angles between the output voltage and current of inverters I and II, respectively, (25) shown at the bottom of the next page.

Fig. 9 presents the angle diagram of inverters I and II. The blue surface represents the angle diagram of inverter I, and the orange surface represents that of inverter II. The green plane represents the zero-angle plane.

As shown in Fig. 10(a), full-range ZVS can be achieved when the angles of both inverters are simultaneously less than $\theta_{\min}$. Fig. 11 presents the ZVS range diagram for inverters I and II. From the calculations and diagram, it is evident that $\theta = 16.5°$ is the critical angle for full-range ZVS. When the angle is less than 16.5°, the system loses full-range ZVS; when the angle exceeds 16.5°, full-range ZVS is achieved. A larger θ allows ZVS across the entire power range, but it also increases the system's reactive power, which reduces the power factor. Moreover, a larger θ results in higher switch currents, which will increase turn-OFF losses.

As shown in Fig. 11, full-range ZVS requires θ greater than 16.5°. To prevent an increase in the system's reactive power due to a larger θ, the angle θ was selected as 21°, based on the experimentally determined parameters, Fig. 10(b) shows the ZVS range, where the green region represents the full-range ZVS area. To determine the relationship between the phase-shift angles over the full range, the ZVS boundary line of inverter I (line1) is derived as shown in (26), and the ZVS boundary line of inverter II (line2) is given in (27)

$$\phi_1 = 0.0022{\phi_2}^2 + 0.4\phi_2 + 33.34 \tag{26}$$

$$\phi_1 = -0.0098{\phi_2}^2 + 2.88\phi_2 - 118. \tag{27}$$

Power adjustment requires modulation from full-load power, necessitating the passage through the zero-phase angle. Two straight lines passing through the origin are selected, and their

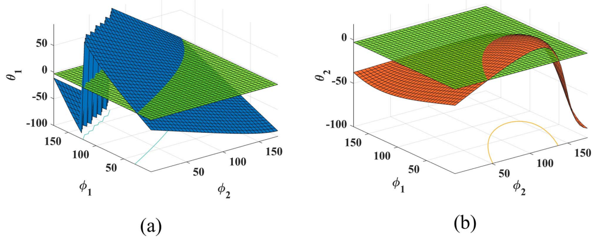

Fig. 9. Angle Diagram. (a) Relationship between θ_1 and the phase shift angle. (b) Relationship between θ_2 and Q, β.

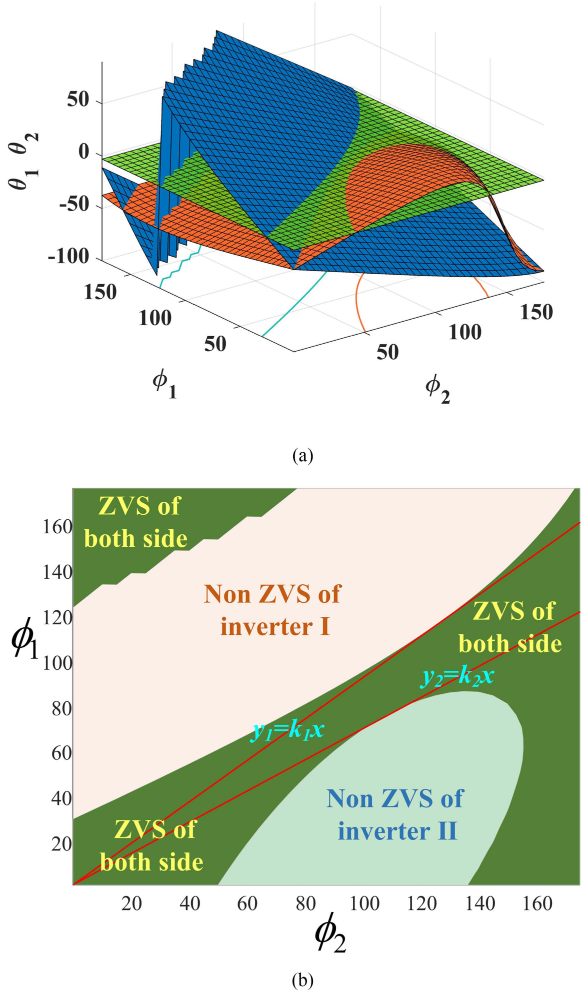

Fig. 10. Range of ZVS. (a) Angle diagram of both Inverters. (b) Full-Range ZVS range of the system ($\theta = 21.7°$).

intersection at the boundaries of line1 and line2 is used to derive the corresponding linear equations, as shown

$$\begin{cases} y_1 = 0.94x \\ y_2 = 0.67x \end{cases}. \tag{28}$$

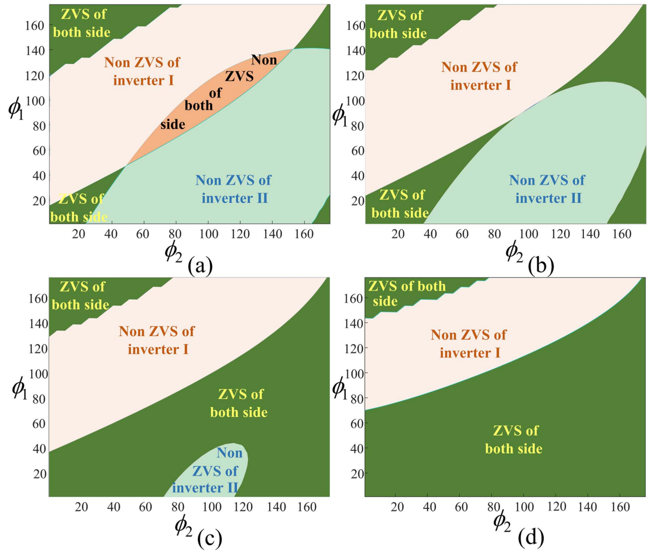

Fig. 11. ZVS Range Diagram of inverters I and II. (a) $\theta = 11.3°$. (b) $\theta = 16.5°$. (c) $\theta = 27°$. (d) $\theta = 46.5°$.

From (28), it can be seen that k_1 and k_2 are 0.97 and 0.64, respectively. To adjust the system's power from full-load conditions, the two phase-shift angles must both begin at zero. Consequently, the system requires the selection of a straight line where$0.67 < k < 0.94$. Additionally, from (20), it is known that the circulating current is minimized when $k = 0.8859$. Based on this, and considering both (28) and (20), a value of $k = 0.9$ is selected as the relationship coefficient for the two phase-shift angles

$$\phi_1 = 0.9\phi_2. \tag{29}$$

E. Power Loss Analysis

Efficiency is a critical factor in the analysis of high-frequency resonant inverters. Therefore, this section presents a detailed analysis of power losses. The power losses in the inverter can be divided into two components: conduction losses and switching losses. These two types of losses significantly influence the efficiency of the inverters, particularly in high-frequency applications [25].

In the IH system proposed in this article, full-range ZVS turn-ON of the switching devices can be achieved. The power losses are primarily concentrated in the conduction losses and turn-OFF losses.

The conduction losses of the switching device can be described as

$$P_{\text{con,loss}} = (I_{s,\text{rms}})^2 R_{\text{on}} \tag{30}$$

$$\begin{cases} \theta_1 = \arctan\left[-\dfrac{1+\beta+(1+\beta)\cos[\phi_1]+2\cos[\phi_1-\phi_2]-Q\sin[\phi_1]-2Q\sin[\phi_1-\phi_2]}{Q+Q\cos[\phi_1]+2Q\cos[\phi_1-\phi_2]+\sin[\phi_1]+\beta\sin[\phi_1]+2\sin[\phi_1-\phi_2]}\right] \\ \theta_2 = \arctan\left[-\dfrac{2+2\beta+\cos[\phi_1-\phi_2]+\cos[\phi_2]+Q\sin[\phi_1-\phi_2]-Q\sin[\phi_2]}{2Q+Q\cos[\phi_1-\phi_2]+Q\cos[\phi_2]-\sin[\phi_1-\phi_2]+\sin[\phi_2]}\right] \end{cases}. \tag{25}$$

where R_{on} is the conduction resistance of the switching device, and $I_{s,\mathrm{rms}}$ is the root mean square current of the switching device.

For the full-bridge converter configuration, the root mean square current of each switch can be described as follows:

$$\begin{cases} I_{s1,\mathrm{rms}} = I_{s2,\ \mathrm{rms}} = I_{s3,\mathrm{rms}} = I_{s4,\mathrm{rms}} = \frac{I_{\mathrm{coil\ 1,rms}}}{2} \\ I_{s5,\mathrm{rms}} = I_{s6,\ \mathrm{rms}} = I_{s7,\mathrm{rms}} = I_{s8,\mathrm{rms}} = \frac{I_{\mathrm{coil\ 2,rms}}}{2} \end{cases} \tag{31}$$

where $I_{s1,\mathrm{rms}}$, $I_{s2,\mathrm{rms}}$, $I_{s3,\mathrm{rms}}$, $I_{s4,\mathrm{rms}}$, $I_{s5,\mathrm{rms}}$, $I_{s6,\mathrm{rms}}$, $I_{s7,\mathrm{rms}}$, $I_{s8,\mathrm{rms}}$ represent the RMS currents of switches S_1, S_2, S_3, S_4, S_5, S_6, S_7, S_8, and $I_{\mathrm{coil1,rms}}$, $I_{\mathrm{coil2,rms}}$ represent the RMS currents of inverters I and II, respectively.

In terms of switching losses, the system enables full-range ZVS turn-ON. Therefore, only turn-OFF losses are considered, and the formula is as follows [26]:

$$P_{\mathrm{off,loss}} \cong \frac{1}{2} V_d I_{\mathrm{off}} t_f f_{\mathrm{sw}}. \tag{32}$$

V_d is the output voltage of the inverter, t_f is the turn-OFF fall time of the switching device, and f_{sw} is the operating frequency of inverter. The turn-OFF losses are primarily related to the turn-OFF current I_{off} of each switching device.

$$\begin{cases} \left|I_{\mathrm{off},S_1}\right| = \left|I_{\mathrm{off},S_2}\right|; \left|I_{\mathrm{off},S_3}\right| = \left|I_{\mathrm{off},S_4}\right| \\ \left|I_{\mathrm{off},S_5}\right| = \left|I_{\mathrm{off},S_6}\right| = \left|I_{\mathrm{off},S_7}\right| = \left|I_{\mathrm{off},S_8}\right| \end{cases}. \tag{33}$$

Therefore

$$\begin{cases} P_{s1,\mathrm{off,loss}} = P_{s2,\mathrm{off,loss}}; P_{s3,\mathrm{off,loss}} = P_{s4,\mathrm{off,loss}} \\ P_{s5,\mathrm{off,loss}} = P_{s6,\mathrm{off,loss}} = P_{s7,\mathrm{off,loss}} = P_{s8,\mathrm{off,loss}} \end{cases}. \tag{34}$$

The formula for the turn-OFF current of the inverter is as follows:

$$\begin{cases} I_{\mathrm{off},I} = A_{\mathrm{peak\ 1}} \sin(\omega t + \theta_1) \\ I_{\mathrm{off},\|} = A_{\mathrm{peak\ 2}} \sin(\omega t + \theta_2) \end{cases} \tag{35}$$

where A_{peak} is the peak current, and θ_1 and θ_2 represent the angles of inverters I and II, respectively. Here, the SiC MOSFET (C3M0021120D) device is used, with a conduction resistance $R_{\mathrm{on}} = 21\,\mathrm{m}\Omega$, $t_{d(\mathrm{off})} = 72\,\mathrm{ns}$ and $\mathrm{t}_f = 25\,\mathrm{ns}$.

Fig. 12 presents the calculation results of the conduction and turn-OFF losses of the system's MOSFETs. These results are obtained from (30) and (32), and satisfy the full-range ZVS dual-phase correlation (29).The dashed line represents the turn-OFF loss of the MOSFETs, and the solid line corresponds to the conduction loss of the MOSFETs. As the phase-shift angle increases, the conduction losses of both inverters progressively decrease. For inverter I, the switching losses of S_1 and S_2 initially increases and then decreases with the increase in angle, while the losses of the other switching devices continue to decrease steadily.

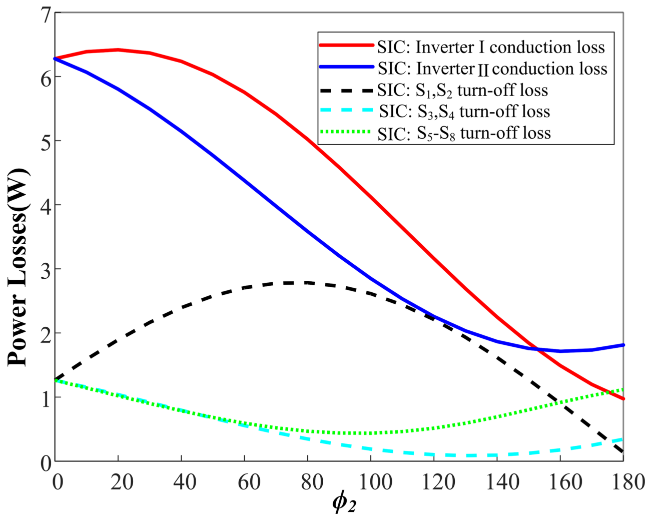

Fig. 12. Power losses of the inverter MOSFET.

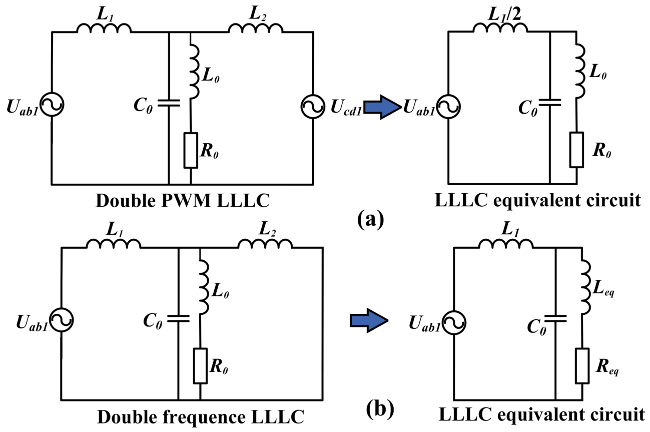

Fig. 13. Equivalent circuit diagram. (a) Dual-port *LLLC*. (b) Single-port *LLLC*.

IV. FREQUENCY-DOUBLING PFM CONTROL UNDER LIGHT LOAD

Since inverter II does not have internal phase-shifting, the system power decreases to $0.25P_{\mathrm{max}}$ once the maximum phase-shift angle is reached. To address this, a frequency-doubling PFM control strategy is employed to adjust the power under light load conditions.

FD-PFM is employed to address the issue of residual power (0.25Pmax) that remains after the dual-phase shift is completed. Therefore, it is crucial to investigate whether the full-load power under the frequency-doubling mode can effectively accommodate the residual power left after the dual-phase shift.

When the system operates in DPS mode, the dual-port inverters simultaneously supply power to the resonant circuits. The inductors L_1 and L_2 are connected in parallel, as shown in the equivalent circuit in Fig. 13(a). In this configuration, U_{ab1} and U_{cd1} represent the fundamental waveforms of the square wave voltages output by inverters I and II, respectively. In frequency-doubling mode, Inverters I and II operate in alternation. Consequently, the operating mode is equivalent to that of a single-end power supply. The equivalent circuit is depicted in Fig. 13(b), with the condition $\omega L \gg R_0$satisfied. The equivalent load for the frequency-doubling single-end power supply mode can be calculated as shown in

$$\begin{cases} R_{\mathrm{eq}} \approx L_1^2 R_0 / (L_0 + L_2)^2 \\ L_{\mathrm{eq}} \approx L_0 L_2 / (L_0 + L_2) \end{cases} \tag{36}$$

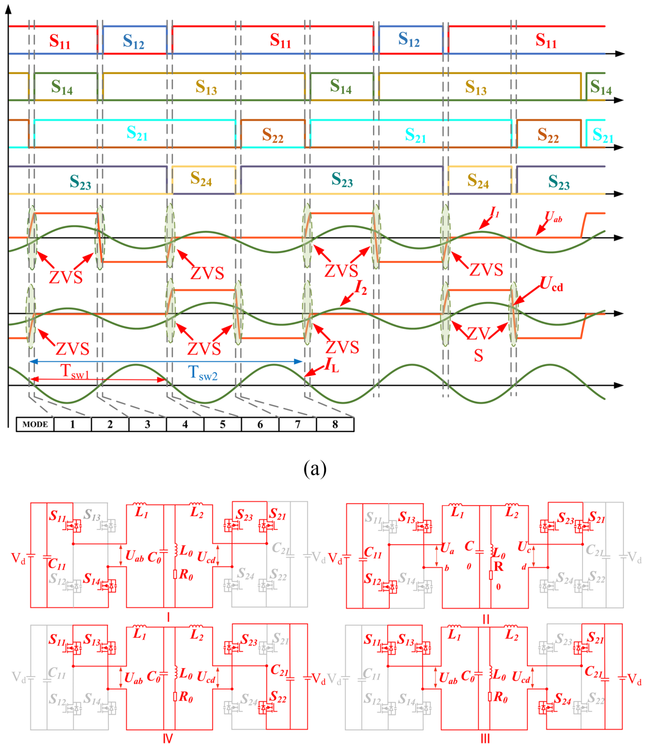

(a)

(b)

Fig. 14. FD operating mode diagram. (a) FD voltage and current waveforms. (b) FD operating mode diagram.

$$\begin{cases} \beta_1 = \frac{L_1}{2L_0} = \frac{1}{2}\beta \\ \beta_2 = \frac{L_1}{L_{\text{eq}}} = 1+\beta \end{cases} \tag{37}$$

where (37) defines the matching coefficients β_1 and β_2 for the dual-port and single-port power supply configurations, respectively. Equation (38) defines the equivalent resistances R_1 and R_2 for the dual-port and single-port power supply configurations, respectively,

$$\begin{cases} R_1 = {\beta_1}^2 R_0 = \frac{1}{4}\beta^2 R_0 \\ R_2 = {\beta_2}^2 R_{\text{eq}} = (1+\beta)^2 R_{\text{eq}} = \beta^2 R_0 \end{cases} \tag{38}$$

$$\begin{cases} P_1 = \left(\frac{2\sqrt{2}V_d}{\pi}\right)^2 * \frac{1}{R_1} = \frac{32{V_d}^2}{\pi^2\beta^2 R_0} \\ P_2 = \left(\frac{2\sqrt{2}V_d}{\pi}\right)^2 * \frac{1}{R_2} = \frac{8{V_d}^2}{\pi^2\beta^2 R_0} \end{cases} \tag{39}$$

where (39) defines P_1 as the full-load power for the dual-port power supply and P_2 as the full-load power for the frequency-doubling single-port power supply. It can be observed that, in the frequency-doubling single-end power supply configuration, the full-load power is one-quarter of the full-load power in the dual-port power supply configuration. This feature can facilitate seamless and smooth power adjustment.

In light-load mode, the system is operated in a frequency-doubling mode. In this mode, inverters I and II alternately supply power to the *LLLC* resonant circuit. When one inverter powers the system, the other inverter forms a freewheeling circuit for the *LLLC* resonant circuit. Fig. 14(a) illustrates the voltage and current waveforms in frequency-doubling mode, while Fig. 14(b) presents the operating mode diagram. In mode I, inverter I supplies power, with switches S_{11} and S_{14} turned ON, resulting in a positive output voltage. Simultaneously, switches S_{21} and S_{23} of inverter II are also turned ON, forming a freewheeling circuit for the system. In mode II, inverter I continues to supply power, with switches S_{12} and S_{13} turned ON, generating a negative output voltage. At this time, switches S_{21} and S_{23} of inverter II remain on, maintaining the freewheeling circuit for the system. In mode III, inverter II exclusively supplies power to the *LLLC* resonant circuit, with switches S_{21} and S_{24} conducting, which results in a positive output voltage from inverter II. Meanwhile, switches S_{11} and S_{13} of inverter I remain continuously conducting, providing a freewheeling circuit for the system. In mode IV, inverter II continues to supply power, with switches S_{22} and S_{23} conducting, producing a negative output voltage. At the same time, switches S_{11} and S_{13} of inverter I remain conducting, thus maintaining the freewheeling circuit for the system. In Fig. 14(a), T_{SW2} denotes the switching period of the inverter, while T_{SW1} represents the period of the resonant circuit. T_{SW2} is observed to be twice as long as T_{SW1}, enabling frequency doubling through the time-division multiplexing of the inverters.

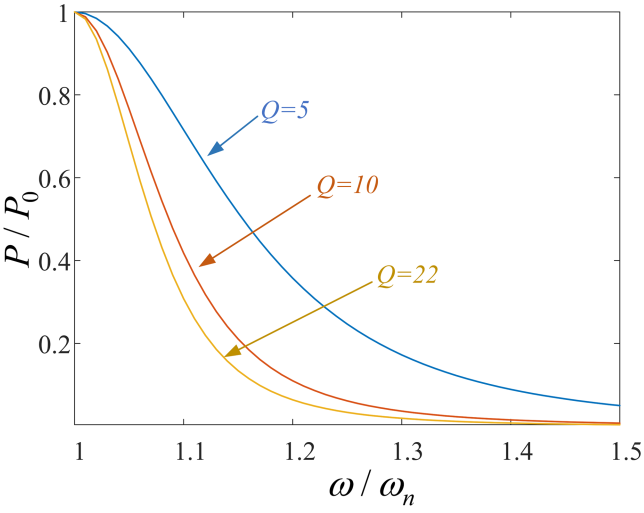

Fig. 15. Output curve of PFM power regulation.

Fig. 15 illustrates the output characteristic curve of PFM power regulation. As the resonant frequency increases, the corresponding quality factor Q of the system also increases. From the figure, it can be observed that as Q becomes larger, the power regulation characteristic curve becomes steeper. Under the same power regulation, the frequency variation in the frequency-doubling mode is smaller. Thus, this article employs the frequency-doubling mode under light-load conditions, resulting in a doubled resonant frequency in the resonant circuit. This approach facilitates a faster power response to frequency variations during PFM power regulation, thereby reducing the range of frequency variation during power adjustment.

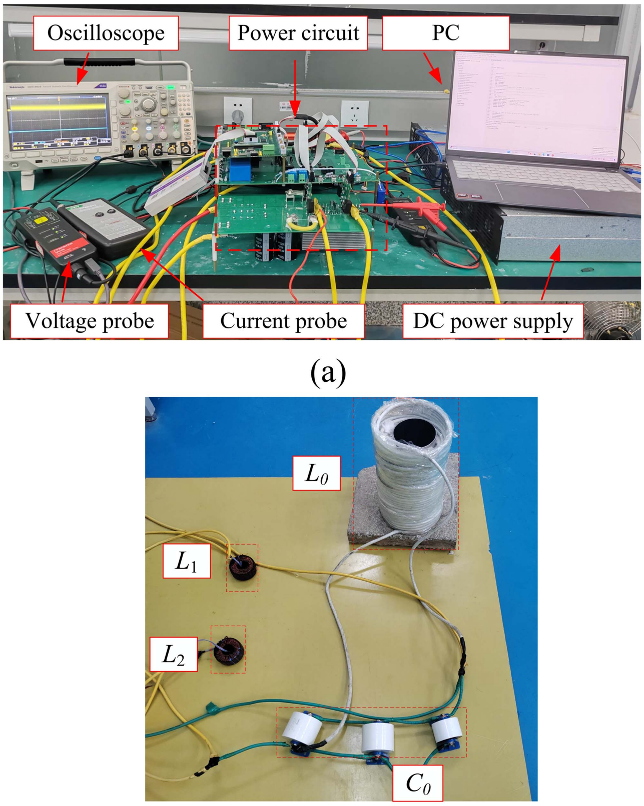

(a)

(b)

Fig. 16. Diagram of the experimental prototype. (a) IH System experimental platform. (b) *LLLC* resonant circuit.

TABLE I
EXPERIMENTAL PARAMETERS OF SYSTEMS

Parameter	Value	Unit
Matching inductor L_1	633	uH
Matching inductor L_2	633	uH
Load inductor L_0	63.3	uH
Load Equivalent Resistance R_0	0.52	Ω
Resonant Capacitor C_0(20kHz)	1.2	uF
Resonant Capacitor C_1(40kHz)	0.3	uF
DC voltage V_d	500	V
Resonant frequency f	20/40	kHz

V. SIMULATION AND EXPERIMENTAL RESULTS

To validate the feasibility of the proposed full-range ZVS control of dual-port *LLLC* system, a 14 kW experimental prototype was developed, as shown in Fig. 16.

The inverter is comprised of SiC MOSFETs (C3M0021120D) and is controlled by a TI TMSF28335 microcontroller. Voltage and current were measured using probes and displayed on a Tektronix MDO3024 oscilloscope. The load parameters were determined using an LCR meter (HIOKI IM3536) to ensure proper load matching. The experimental parameters are given in Table I.

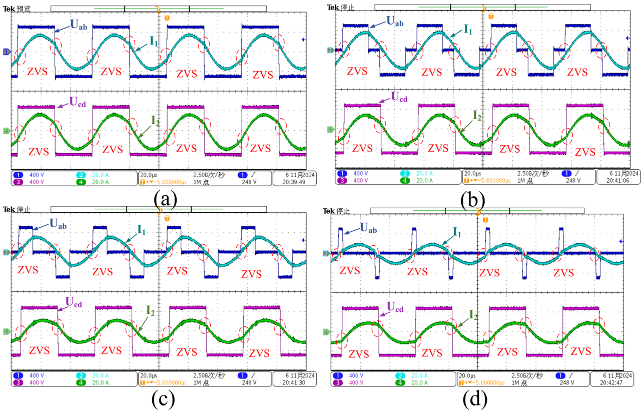

(a) (b)

(c) (d)

Fig. 17. Experimental results of voltage and current waveforms. (a) $\phi_1 = 0°$, $\phi_2 = 0°$. (b) $\phi_1 = 54°$, $\phi_2 = 60°$. (c) $\phi_1 = 108°$, $\phi_2 = 120°$. (d) $\phi_1 = 162°$, $\phi_2 = 180°$.

Fig. 17 presents the experimental voltage and current waveforms generated by inverters I and II under different phase-shift angles. The resonant frequency is 20 kHz.

Fig. 17(a) depicts the voltage and current waveforms at a phase-shift angle of 0°. The graph shows that the currents of both inverters I and II consistently lag behind the voltage by a constant phase-angle. The entire system remains in an inductive state and continuously operates in ZVS mode. Fig. 17(b) shows the voltage and current waveforms for $\phi_1 = 54°$, $\phi_2 = 60°$. The presence of phase-shift angle ϕ_1 results in a continuous decrease in the duty cycle of the inverter output voltage. Simultaneously, phase-shift angle ϕ_2 causes a reduction in the output currents of both inverters I and II. Furthermore, the current I_2 shows a phase lag relative to I_1. Fig. 17(c) and (d) present the experimental results for $\phi_1 = 108°$, $\phi_2 = 120°$and $\phi_1 = 162°$, $\phi_2 = 180°$, respectively. These results show that the duty cycle of the inverter's voltage U_{ab} decreases continuously, along with a corresponding reduction in the currents I_1 and I_2 . Additionally, the system is operated consistently in the ZVS state. As the phase-shift angle increases, the power output gradually diminishes. These experimental findings align with the theoretical analysis.

Fig. 18 presents the experimental results of ZVS for inverters I and II under varying dual phase-shift angles. U_{ds11} represents the voltage of S_{11}, while U_{ds21} represents the voltage of S_{21}. From the figure, it is clear that as the dual phase-shift angle increases, the system consistently operates in the ZVS state. Fig. 19 shows the experimental results of the output currents I_1, $I_{2,}$ and I_L. As the phase-shift angle increases, the magnitudes of I_1 and I_2 decrease, while the phase difference between them increases.

Fig. 20 presents the power adjustment experiments under different dual-phase shift conditions. As shown in the figure, during the phase angle switching process, the system can operate at the resonant frequency point stably due to the action of the PLL.

FD-PFM control strategy is used under light load conditions. Fig. 21 shows the FD-PFM experimental waveforms. In the figure, T_{sw2} represents the switching period of the inverter,

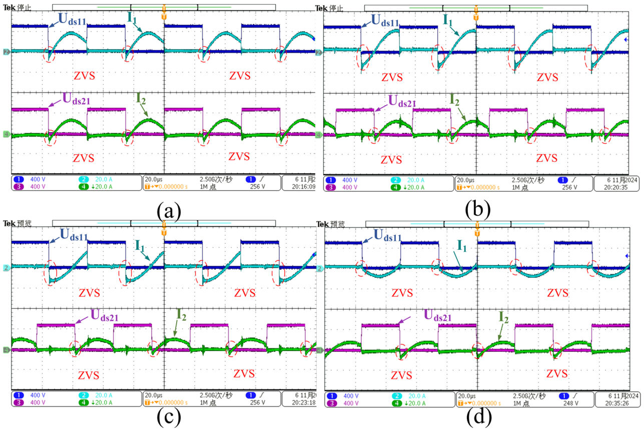

Fig. 18. Experimental results of ZVS. (a) $\phi_1 = 0°$, $\phi_2 = 0°$. (b) $\phi_1 = 54°$, $\phi_2 = 60°$. (c) $\phi_1 = 108°$, $\phi_2 = 120°$. (d) $\phi_1 = 162°$, $\phi_2 = 180°$.

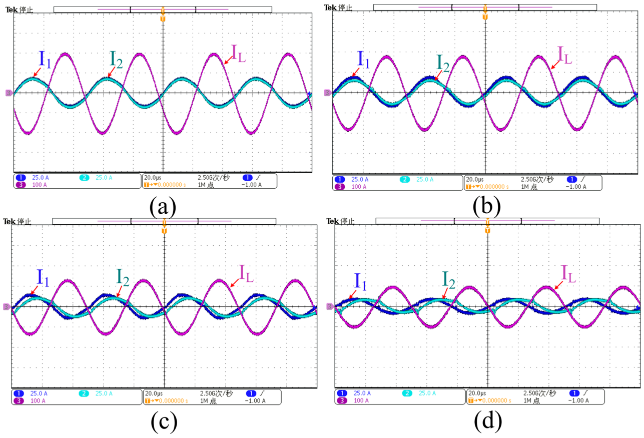

Fig. 19. Inverter output current waveform. (a) $\phi_1 = 0°$, $\phi_2 = 0°$. (b) $\phi_1 = 54°$, $\phi_2 = 60°$. (c) $\phi_1 = 108°$, $\phi_2 = 120°$. (d) $\phi_1 = 162°$, $\phi_2 = 180°$.

while T_{sw1} denotes the period of the resonant circuit. As shown in Fig. 21(a), inverter I operates for one T_{sw1} period and then stops, while inverter II alternates during the subsequent T_{sw1} period. Inverters I and II time-share in this manner. At this point, the inverter switching frequency is $f_{sw\,2} = 20\,\mathrm{kHz}$, and the resonant circuit operates at a frequency $f_{sw\,1} = 2f_{sw\,2}$. This configuration achieves frequency doubling for the load while the inverters keep the switching frequency constant. Fig. 21(b) illustrates the ZVS effect, with the system continuously operating in the ZVS state.

Fig. 22 illustrates the frequency-doubling PFM mode. As the frequency increases, the phase difference between the voltage and current also increases, and the power continuously decreases.

Fig. 23 illustrates the circulating currents under different control strategies. It can be observed that the circulating current of the proposed DPS control strategy is the smallest. The circulating currents of the signal phase shift (SPS) [27], extended phase shift (EPS) [28], and triple phase shift (TPS) [29] control strategies are all larger than that of the DPS control strategy, with TPS exhibiting the largest circulating current. Although PFM does not generate circulating currents, it exhibits relatively high reactive power.

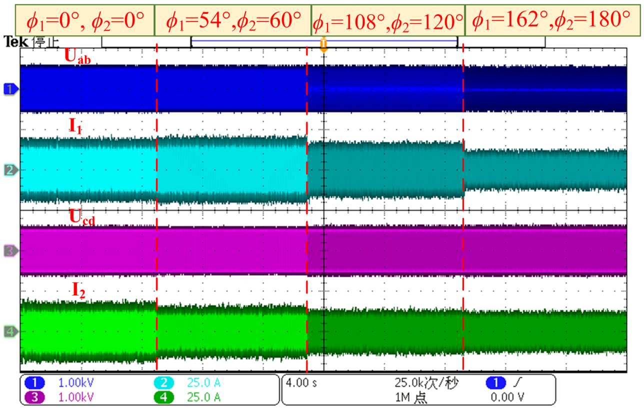

Fig. 20. DPS power modulation diagram.

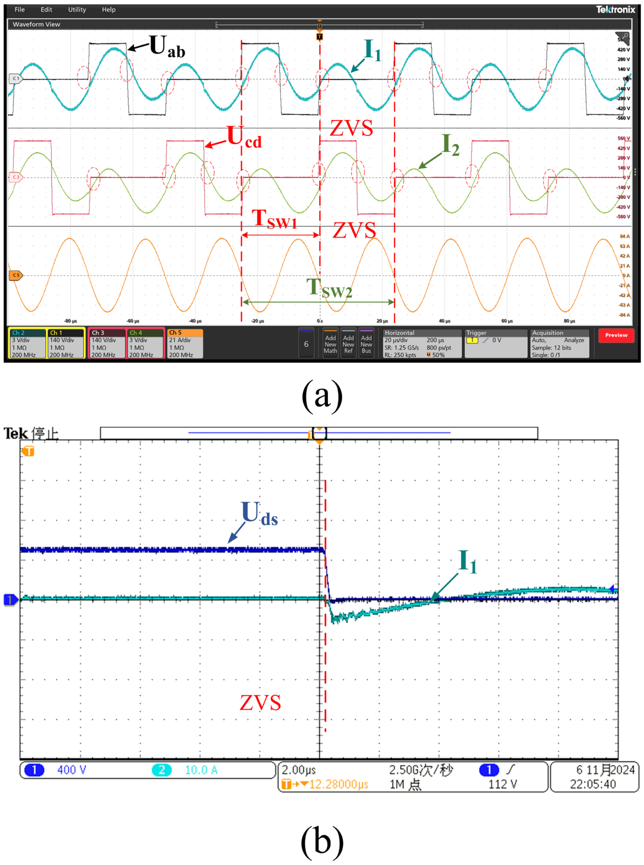

Fig. 21. Frequency doubling experimental waveform. (a) Voltage and current waveforms. (b) ZVS effect.

Fig. 24 presents a comparison of the actual efficiency of the proposed DPS with the control strategies of SPS, TPS, EPS, and PFM. From the figure, it is clear that when $P > 0.25P_{\max}$, the system can operate continuously in the ZVS state under the DPS control strategy. The system achieves a maximum efficiency of 95.5%, and within the power range of $0.25P_{\max}$-$P_{\max}$, the efficiency remains between 92% and 95.5%

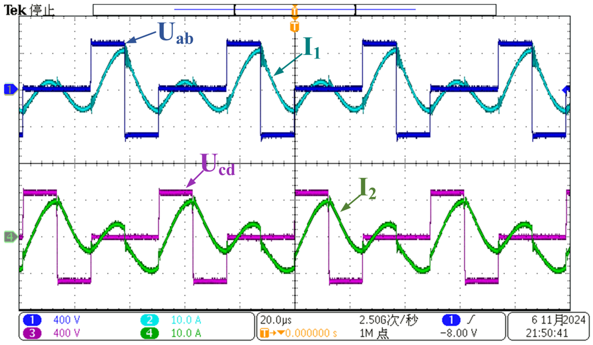

Fig. 22. Frequency-doubling PFM power control.

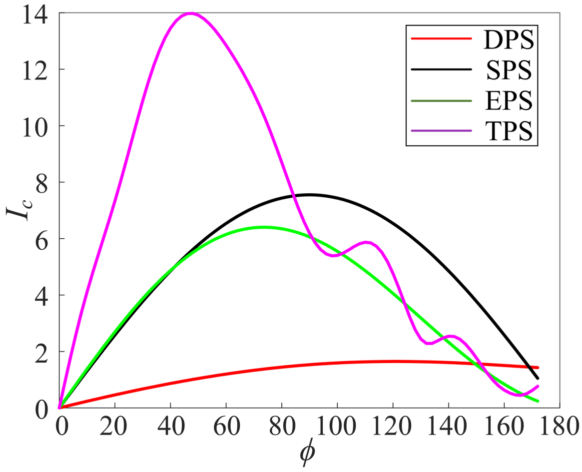

Fig. 23. Comparison of circulating currents.

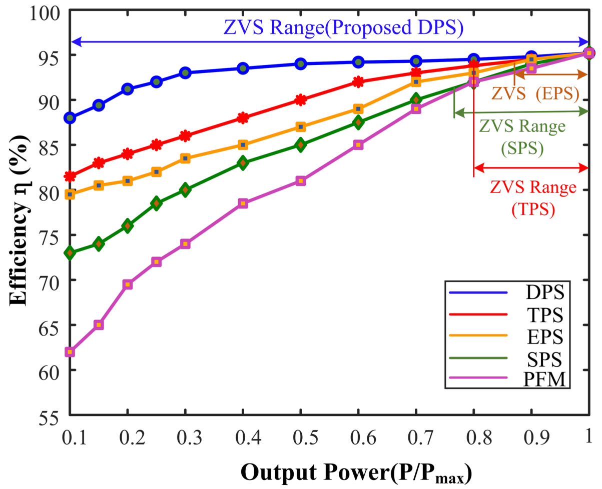

Fig. 24. Efficiency comparison.

. When $P < 0.25P_{\max}$, the system is switched to the FD- PFM mode. In this mode, the range of frequency change during power regulation is significantly reduced, and the system remains in the ZVS state. Consequently, under light load conditions, the efficiency of system maintains above 87%, with the entire modulation process IH power systems operating in the ZVS state. In contrast, the ZVS range of the SPS, TPS, and EPS strategies is relatively narrow. As shown in the figure, its ZVS range of SPS is confined to $0.75P_{\max}$-$P_{\max}$. Outside this range, ZVS is lost, resulting in efficiency decreased. The ZVS range of EPS is the smallest, followed by TPS, with neither achieving ZVS across the entire range. While PFM can achieve ZVS across the entire range, its frequency increases continuously during power adjustments, and the phase angle between voltage and current also increases. This leads to higher reactive power and the lower efficiency.

VI. CONCLUSION

A comprehensive control strategy of dual-port *LLLC* IH system is proposed, which can ensure ZVS operation across the full power range. DPS control strategy is proposed to overcome the limited ZVS range. By analyzing the minimum circulating current of two inverters and the operation range of ZVS, the optimal mathematical relationship between the two phase-shift angles of system is obtained. To achieve ZVS operation across the full power range, a frequency-doubled PFM control strategy is proposed under one-quarter of the total full-load power. This allows power regulation within a narrower frequency range under light load. Experimental results from a test prototype confirm that the experimental findings align well with theoretical predictions, demonstrating that ZVS can be achieved across the entire power range, and the system consistently can operate with high efficiency.

REFERENCES

[1] S. Inami and S. Komeda, “A three-phase AC input induction heating system with heat distribution control capability,” *IEEE Trans. Ind. Electron.*, vol. 72, no. 3, pp. 2199–2209, Mar. 2025.

[2] H. Sarnago, J. M. Burdio, and O. Lucia, “Dual-output extended-power-range quasi-resonant inverter for induction heating appliances,” *IEEE Trans. Power Electron.*, vol. 38, no. 3, pp. 3385–3397, Mar. 2023.

[3] M. S. Huang, J. C. Hu, Y. M. Chen, Z. F. Li, and C. W. Lin, “Simple power control method for induction heating cookers using fundamental frequency power under asymmetrical pulse-width modulation,” *IEEE Trans. Power Electron.*, vol. 40, no. 4, pp. 5094–5108, Apr. 2025.

[4] X. Ren, Y. Jiang, H. Weng, T. Long, and D. Xu, “Design and testing of a soft-switching solid-State transformer module,” *IEEE J. Emerg. Sel. Topics Power Electron.*, vol. 12, no. 6, pp. 5977–5989, Dec. 2024.

[5] C. W. Chang and D. Dong, “Enhanced *di/dt*-RC sensing structure for accurate dynamic current measurement in paralleled SiC MOSFETs,” *IEEE Trans. Power Electron.*, vol. 40, no. 7, pp. 9492–9506, Jul. 2025.

[6] L. Tang et al., “Influence of mismatched gate loop inductance on threshold dispersity evolution and current sharing of parallel SiC MOSFETs,” *IEEE Trans. Power Electron.*, vol. 40, no. 5, pp. 6921–6932, May 2025.

[7] Y. He, X. Wang, S. Shao, and J. Zhang, “Active gate driver for dynamic current balancing of parallel-connected SiC MOSFETs,” *IEEE Trans. Power Electron.*, vol. 38, no. 5, pp. 6116–6127, May 2023.

[8] J. Wang, F. Ma, Q. Yang, Z. Zhang, G. Huang, and S. Fan, “A high-power two-port multiple-frequency LLLC induction heating power system,” *IEEE Trans. Power Electron.*, vol. 40, no. 1, pp. 1234–1246, Jan. 2025.

[9] J. Egalon, S. Caux, P. Maussion, M. Souley, and O. Pateau, “Multiphase system for metal disc induction heating: Modeling and RMS current control,” *IEEE Trans. Ind. Appl.*, vol. 48, no. 5, pp. 1692–1699, Sep./Oct. 2012.

[10] T. Mishima, C. Takami, and M. Nakaoka, “A new current phasor-controlled ZVS twin half-bridge high-frequency resonant inverter for induction heating,” *IEEE Trans. Ind. Electron.*, vol. 61, no. 5, pp. 2531–2545, May 2014.

[11] H. N. Pham, H. Fujita, K. Ozaki, and N. Uchida, “Dynamic analysis and control for resonant currents in a zone-control induction heating system,” *IEEE Trans. Power Electron.*, vol. 28, no. 3, pp. 1297–1307, Mar. 2013.

[12] R. C. M. Gomes, M. A. Vitorino, D. A. Acevedo-Bueno, and M. B. R. Corrêa, “Multiphase resonant inverter with coupled coils for AC–AC induction heating application,” *IEEE Trans. Ind. Appl.*, vol. 56, no. 1, pp. 551–560, Jan./Feb. 2020.

[13] R. Gu, D. Zhang, J. Duan, W. Zhang, and A. Li, “A reconfigurable current-fed LLC resonant converter with circulant PWM control and wide gain range,” *IEEE Trans. Ind. Electron.*, vol. 72, no. 4, pp. 3575–3586, Apr. 2025.

[14] T. Gao et al., “Research on current sharing control method based on duty cycle regulation for interleaved parallel LLC resonant converters,” *IEEE J. Emerg. Sel. Topics Power Electron.*, vol. 12, no. 4, pp. 3977–3985, Aug. 2024.

[15] Q. Yang et al., “A comprehensive induction heating power system for large all-metal cooking pots with energy storage,” *IEEE J. Emerg. Sel. Topics Ind. Electron.*, vol. 13, no. 2, pp. 1916–1927, Apr. 2025, doi: 10.1109/JESTPE. 2024. 3507949.

[16] D. N. Sankhe, R. R. Sawant, and Y. S. Rao, “FPGA-based hybrid control strategy for resonant inverter in induction heating applications,” *IEEE J. Emerg. Sel. Topics Ind. Electron.*, vol. 3, no. 1, pp. 156–165, Jan. 2022.

[17] T. P. Kumar Gautam and A. Bhattacharya, “High-frequency soft switching one stage conversion using PWM and PDM control technique for induction heating application,” in *Proc. Int. Conf. Recent Trends Comput. Sci. Technol.*, 2024, pp. 706–711.

[18] T. Luo et al., “An optimal VF-TPS modulation scheme for CLLC converter with minimized RMS current,” *IEEE Trans. Power Electron.*, vol. 40, no. 3, pp. 4170–4185, Mar. 2025.

[19] R. Moriyasu, Y. Noge, M. Shoyama, and M. S. Hassan, “Surge current reduction in LLC resonant converter with a hybrid control strategy of PFM and PSM for expansion of output voltage range,” in *Proc. IEEE Appl. Power Electron. Conf. Expo.*, 2023, pp. 2747–2752.

[20] S. Chudjuarjeen, A. Sangswang, and C. Koompai, “An improved LLC resonant inverter for induction-heating applications with asymmetrical control,” *IEEE Trans. Ind. Electron.*, vol. 58, no. 7, pp. 2915–2925, Jul. 2011.

[21] T. Mishima and M. Nakaoka, “A load-power adaptive dual pulse modulated current phasor-controlled ZVS high-frequency resonant inverter for induction heating applications,” *IEEE Trans. Power Electron.*, vol. 29, no. 8, pp. 3864–3880, Aug. 2014.

[22] J. Zhou, H. Liu, X. Xu, Y. Wang, and T. Zhao, “SiC MOSFET solid-State circuit breaker-based motor control center: Design analysis, novel soft start and soft turn-off strategies,” *IEEE J. Emerg. Sel. Topics Power Electron.*, early access, doi: 10.1109/JESTPE. 2024. 3522766.

[23] M. Chen, L. Jia, B. Li, D. Zhang, and F. Jiang, “A novel CTTC structure and optimization design method for CLLC bidirectional resonant converter,” *IEEE Trans. Power Electron.*, vol. 40, no. 6, pp. 7800–7813, Jun. 2025.

[24] V. Esteve et al., “Improving the reliability of series resonant inverters for induction heating applications,” *IEEE Trans. Ind. Electron.*, vol. 61, no. 5, pp. 2564–2572, May 2014.

[25] X. Xue, Z. Liu, W. Li, and H. Su, “Design of a single-stage dual active bridge microinverter with wide load adaptability based on loss optimization,” *IEEE Trans. Power Electron.*, vol. 40, no. 6, pp. 7919–7935, Jun. 2025.

[26] H. P. Park and J. H. Jung, “Load-adaptive modulation of a series-resonant inverter for all-metal induction heating applications,” *IEEE Trans. Ind. Electron.*, vol. 65, no. 9, pp. 6983–6993, Sep. 2018.

[27] S. Mandal, A. Shukla, and S. Doolla, “Multiswitch-leg DAB converter for low dv/dt at high operating frequency for MVDC systems,” *IEEE Trans. Power Electron.*, vol. 39, no. 10, pp. 12170–12176, Oct. 2024.

[28] L. Gong et al., “An ultrafast and wide-safe-range start-up method of DAB converters with straightforward frequency-phase closed-loop control,” *IEEE Trans. Power Electron.*, vol. 39, no. 11, pp. 14161–14166, Nov. 2024.

[29] G. Park, H. Kim, B. G. Cho, and S. Cui, “ZVS-enhanced and RMS-current-minimized optimal modulation scheme of Dual-active bridge converter with comprehensive ZVS analysis,” *IEEE Trans. Power Electron.*, vol. 40, no. 7, pp. 9004–9018, Jul. 2025.

Qixiang Yang was born in Henan, China, in 1995. He received the B.S. and M.S. degrees in electrical engineering from Henan Polytechnic University, Jiaozuo, China, in 2018 and 2021, respectively. He is currently working toward the Ph.D. degree in electrical engineering with the College of Electrical and Information Engineenng, Hunan University, Changsha, China.

His research interests include power electronic transmission and High-frequency resonant converter.

Fujun Ma (Senior Member, IEEE) was born in Hunan, China, in 1985. He received the B.S. degree in automation and the Ph.D. degree in electrical engineering from Hunan University, Changsha, China, in 2008 and 2015, respectively.

Since 2020, he has been a Professor with the College of Electrical and Information Engineering, Hunan University. His research interests include power quality managing technique of electrified railway.

Zhengxiao Zhang was born in Guangxi, China in 2001. He received the bachelor’s degree in electrical engineering from Guangxi University, Nanning, China, in 2023. He is currently working toward the master’s degree in electrical engineering with the School of Electrical and Information Engineering, Hunan University, Changsha, China.

His main research interests are power electronic transmission and high frequency induction heating.

Junpan Wang was born in Yueyang, Hunan, China, in 2000. He received the B.S. degree in electrical engineering from the Changsha University of Science & Technology, Changsha, China, in 2022. He is currently working toward the M.S. degree in electrical engineering with Hunan University, Changsha, China.

His current research interests include induction heating converter.

Gelin Huang was born in Hunna, China, in 1997. He received the B.S degree in electrical engineering from Hunan University, Changsha, China, in 2019, where he is currently working toward the Ph.D. degree in electrical engineering with the College of Electrical and Information Engineering.

His research interests include modular multilevel converters impedance modeling, loss analysis and optimal control.

Rui Fan was born in Maanshan, Anhui, China, in 1999. He received the B.S. degree in electrical engineering from Hefei University of Technology, Hefei, China, in 2022. He is currently working toward the M.S. degree in electrical engineering with Hunan University, Changsha, China.

His current research interests include power electronics and High-frequency resonant converter.

Quanjie Li received the B.S. degree in electrical engineering from Hunan University of Science and Technology, Xiangtan, China, in 2020, the M.S. degree in electrical engineering from Yanshan University, Qinhuangdao, China, in 2023. He is currently working toward the Ph.D. degree in electrical engineering with Hunan University, Changsha, China.

His current research interests include high-frequency resonant converters.

Zhiheng Tong was born in Anhui, China, in 2002. He received the B.S. degree in electrical engineering from Hefei University of Technology, Hefei, China, in 2024. He is currently working toward the M.S. degree in electrical engineering with Hunan University, Changsha, China.

His main research interests are power electronic transmission and high-frequency induction heating.